High-resolution electron energy-loss spectroscopy of $BaTiO_3/SrTiO_3$ multilayers

Jingmin Zhang,[1] Alina Visinoiu,[2] Frank Heyroth,[1] Frank Syrowatka,[1] Marin Alexe,[2] Dietrich Hesse,[2] and Hartmut S. Leipner[1,*]

[1]*Martin-Luther-Universität Halle-Wittenberg, Interdisziplinäres Zentrum für Materialwissenschaften, Hoher Weg 8, D-06120 Halle, Germany*

[2]*Max-Planck-Institut für Mikrostrukturphysik, Weinberg 2, D-06120 Halle, Germany*

(Received 31 May 2004; revised manuscript received 17 August 2004; published 23 February 2005)

The dielectric properties of $BaTiO_3$ thin films and multilayers are different from bulk materials because of nanoscale dimensions, interfaces, and stress-strain conditions. In this study, $BaTiO_3/SrTiO_3$ multilayers deposited on $SrTiO_3$ substrates by pulsed laser deposition have been investigated by high-energy-resolution electron energy-loss spectroscopy. The fine structures in the spectra are discussed in terms of crystal-field splitting and the internal strain. The crystal-field splitting of the $BaTiO_3$ thin layer is found to be a little larger than that of bulk $BaTiO_3$, which has been interpreted by the presence of the internal strain induced by the misfit at the interface. This finding is consistent with the lattice parameters of the $BaTiO_3$ thin layer determined by the selected area diffraction pattern. The near-edge structure of the oxygen K edge in $BaTiO_3$ thin layers and in bulk $BaTiO_3$ are simulated by first-principle self-consistent full multiple-scattering calculations. The results of the simulations are in a good agreement with the experimental results. Moreover, the aggregation of oxygen vacancies at the rough $BaTiO_3/SrTiO_3$ interface is indicated by the increased [Ti]/[O] element ratio, which dominates the difference of dielectric properties between $BaTiO_3$ layer and bulk materials.

DOI: 10.1103/PhysRevB.71.064108 PACS number(s): 79.20.Uv, 77.55.+f, 68.65.Ac, 68.37.Lp

I. INTRODUCTION

Ferroelectric thin films are used for the development of next generation microwave controllers, frequency-agile filters, voltage-controlled oscillators, tunable microwave filters, nonvolatile random access memories, etc.[1] The dielectric permittivity can be controlled by applying a sufficiently high electric field. This field can be easily achieved in thin film structures using low control voltages below 50 V, which is necessary for high-density integrated electric devices. Recent investigations have been focused on barium strontium titanate $(Ba,Sr)TiO_3$ (BST) because of its high permittivity and specific capacitance. One of the most promising applications of BST is the use for very-high-density dynamic random access memories (DRAMs).[2] High integration requires very small sizes of the electric devices, but the dielectric properties of many existing materials are different at nanoscale dimensions.

In order to grow high quality thin films on a certain substrate, many techniques have been developed. Among them, pulsed laser deposition (PLD) is widely and successfully used. High-quality ceramic thin films can be obtained by PLD with carefully optimized oxygen pressure, substrate temperature, and laser spot size, as well as other parameters such as pulse repetition rate.

Electron energy-loss spectroscopy (EELS) coupled with a scanning transmission electron microscope (STEM) is becoming an important nanoanalytical technique in materials science. Due to the identical physical mechanism to x-ray absorption spectroscopy (XAS) of excitation of core-shell electrons, EELS can be used as a complemental technique, especially in the low-energy region (<1000 eV), i.e., EELS has similar abilities as soft XAS. The most promising advantage of EELS and/or STEM is the nanosize probe and the high intensity of the signals with respect to XAS or EELS applied in conventional transmission electron microscopy. Therefore, EELS and/or STEM has been widely used for investigations of electric properties and chemical composition in nanoscale regions, such as interfaces,[3–5] grain boundaries,[6–8] and dislocation cores.[9,10]

$BaTiO_3/SrTiO_3$ (BTO/STO) multilayers are promising in view of their unique properties different from thin films and bulk materials.[11] The dielectric properties of BTO/STO multilayers are mainly determined by the crystallization of the BTO layers and the interfaces between the BTO and STO layers. In this study, fine structures of the titanium L_{23} edge and the oxygen K edge are investigated by EELS and/or STEM in multilayers consisting of BTO/STO layers deposited on $SrTiO_3$ (001) substrates by PLD.

II. EXPERIMENT

Two series of multilayer films were deposited on $SrTiO_3$ (001) substrates in the sequences STO (50 nm)/BTO (10 nm) and STO (100 nm)/BTO (10 nm) by PLD, respectively, as shown in Figs. 1(a) and 1(b). Details of the growth and the transmission electron microscopy (TEM) preparation of the specimens studied in this work were similar to those described in Ref. 12. The electron energy-loss (EEL) spectra were acquired by a dedicated STEM (VG HB 501 UX, vacuum generators) equipped with a cold field-emission gun (FEG) and a new Gatan parallel EELS spectrometer (Enfina 1000). The STEM was operated at 100 keV. The operating pressure was $\sim 5.0\times10^{-9}$ m bar in the column and $\sim 3.0\times10^{-11}$ m bar in the FEG chamber. Both dark count readout and channel-to-channel variation in gain response were corrected by the corresponding standard procedures. The background of the spectrum was removed by the AE^{-r}

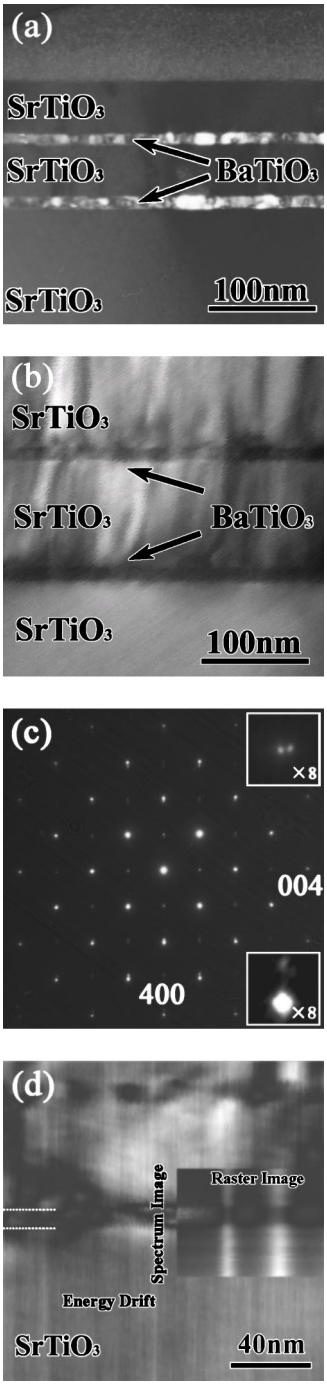

FIG. 1. (a) Cross-sectional TEM dark-field image of the multilayers consisting of STO (50 nm)/BTO (10 nm). (b) Cross-sectional STEM bright-field image of the multilayers consisting of STO (100 nm)/BTO (10 nm). (c) Selected area diffraction pattern from the interface region between the $BaTiO_3$ film and the $SrTiO_3$ substrate. The reflections from the (400) and (004) planes are magnified 8 times in the insets. (d) EEL spectra line-scan acquisition across a BTO layer. The energy drift was continuously monitored at the marked position. The white arrow indicates the scanning direction. The upper and lower interfaces are indicated by dashed white lines. The raster image, consisting of a series of spectra, is shown in the inset.

power-law extrapolation of the pre-edge of the core-loss edge,[13] where the coefficient A determines the intensity of the background, the exponent r (generally in the range 2–6) is responsible for the curvature of the fitting curves, and E denotes the energy loss. The energy resolution of the coupled microscope and spectrometer, determined from the full width at half maximum (FWHM) of the zero-loss peak (ZLP), was about 0.4 eV. The beam current focused on the specimen was ~1 nA. The spatial resolution of the coupled microscope and spectrometer estimated by a line scan across a sharp edge was about 1.0 nm. An entrance aperture of 2 mm was selected for collecting inelastic electrons. The uncalibrated collection semiangle, which is determined by the radius of the spectrometer entrance aperture and the distance from the specimen to the collection aperture, was ~6.5 m rad. The collection semiangle should be calibrated prior to the analysis of the element ratio, however, because the atomic ratio is a function of the collection angle.[13] Because the specimen is immersed in the field of the objective lens in the dedicated STEM, the postspecimen field produces an angular compression of the transmitted electron beam. Therefore, the actual collection semiangle is somewhat larger than the uncalibrated value. The collection angle can be calibrated by projecting the spectrometer entrance aperture into the plane of the diffraction pattern of a known crystalline specimen to obtain the so-called "effective diameter" of the spectrometer entrance aperture.[14] The calibrated collection semiangle amounts to about 12 m rad in the used STEM. The collection angle is large enough to collect most of the inelastically scattered electrons since the characteristic scattering angle is usually very small. For optimizing the probe size with a sufficient beam current, a 50 μm objective aperture is used to restrict the convergent semiangle (~14 m rad).

The DIGITALMICROGRAPH 3.7.1 software package was used to control the automatic EELS acquisition, including qualitative and quantitative analysis. A plug-in tool and a script class, based on the DIGITALMICROGRAPH software development kit and script language, were developed to facilitate the processing of the spectra.

III. RESULTS AND DISCUSSION

The cross-sectional TEM dark-field image and STEM bright-field image of the multilayers are shown in Figs. 1(a) and 1(b), respectively. Fig. 1(c) gives the selected area diffraction (SAD) pattern taken from the region, including both the substrate and the $BaTiO_3$ layer with the incident electron beam parallel to the [010] direction. The orientation relationship between BTO layers and the STO substrate can be obtained from the diffraction pattern: (001) BTO$\|$(001) STO, and [100] BTO$\|$[100] STO. The [400] and [004] reflections (magnified in the insets) from $BaTiO_3$ and $SrTiO_3$ are well separated. The sharp reflections confirm that the $BaTiO_3$ layer is a high-quality single-crystal layer. Because the lattice parameter (a=3.905 Å, Ref. 16) of the $SrTiO_3$ substrate is stable and known very well, the reflections from $SrTiO_3$ can be used as a standard ruler to determine the lattice parameters of the $BaTiO_3$ layer without calibration of the camera length. The calculated lattice parameters of the $BaTiO_3$ lay-

TABLE I. Lattice parameters (a, b, and c) of a 10-nm-thick $BaTiO_3$ layer. For comparison, the data of a 12-nm-thick $BaTiO_3$ thin film[11] and bulk $BaTiO_3$ (Ref. 15) are given. V is the volume of the unit cell.

	BTO layer (10 nm)	BTO film (12 nm)	Bulk BTO
c (Å)	4.055	4.16	4.038
a, b (Å)	3.930	3.95	3.994
$V^{1/3}$ (Å)	3.970	4.02	4.008
c/a	1.032	1.053	1.011

ers are summarized in Table I. The lattice parameter a is close to that of a 12-nm-thick $BaTiO_3$ single layer deposited on a $SrTiO_3$ substrate reported by Yoneda *et al.*[11] But the lattice parameter c in Ref. 11 might be overestimated since the volume of the unit cell should be a little smaller than that of bulk $BaTiO_3$ due to the presence of misfit strain. (Note that the lattice parameter a of the STO substrate is 2.3% smaller than that of bulk BTO.) From Table I, one can see that the lattice parameter is shortened in the growth plane and elongated along the growth direction (c axis) by the strain at the interfaces. In comparison with the $BaTiO_3$ thin film, the smaller lattice parameter in the growth plane indicates that the internal strain is stronger in the $BaTiO_3$ layer than in the thin film due to the deposited $SrTiO_3$ film.

A. Ti L_{23} edge

The ferroelectric properties of $BaTiO_3$ layers are related to the distortion of oxygen octahedra.[17] Although the lattice parameters can be obtained from the SAD pattern, the atomic positions within the unit cell cannot be extracted in a similar way. The ligand-field multiplet model has been successfully applied to identify the symmetry of oxygen octahedra in transition metal compounds.[18] It is derived that multiplet effects dominate the profile of the Ti L_{23} near-edge structure in titanate perovskites. The density of unoccupied states of the Ti atoms are sensitive to short-range coordination. The four well split peaks in the Ti L_{23} edge are attributed to excitations of $2p_{3/2}$ and $2p_{1/2}$ subshells to unoccupied t_{2g} and e_g states.[19] Peak positions, FWHM, asymmetry of the peak shape, satellite structures, and branch ratios[20] contain information about the atomic arrangement. As well known, bulk $BaTiO_3$ is found in a cubic perovskite phase above the Curie point (T_c=120 °C) and in a tetragonal phase at room temperature (cf. Fig. 2). The Ti atom lies in the center of the regular octahedron of oxygen atoms in the cubic perovskite structure, while the octahedron of oxygen atoms is distorted along the c axis in the tetragonal perovskite structure.

Thirty spectra were acquired along the direction indicated by the white arrow in Fig. 1(d). The acquisition time per spectrum was set to 10 s. A small spatial drift of the specimen, due to a local charging effect, was corrected by the help of the raster image [inset in Fig. 1(d)]. The $BaTiO_3$ layer of definite thickness can be used as a ruler mark. Thus, the position of the acquired spectrum can be corrected, assuming a continuous drift of the specimen along the line-scan direction. The average scanning step corrected by this method

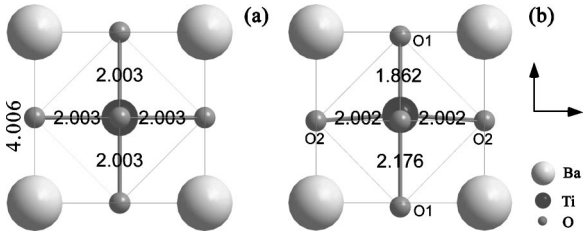

FIG. 2. (a) Cubic perovskite structure of bulk $BaTiO_3$ above the Curie point. (b) Tetragonal perovskite structure of bulk $BaTiO_3$ at room temperature. The labeled lattice parameters and bond lengths are given in Å.

amounts to about 1 nm, which is close to the estimated probe size. In order to correct the intrinsic energy drift of the electron beam, the zero-loss peak was monitored at the position marked in Fig. 1(d); however, this method can only limit the energy drift below ±0.3 eV because of the slight asymmetry of the zero-loss peak. Therefore, all EEL spectra contained in the raster image were normalized and energetically aligned by the t_{2g} peak in the L_3 edge, which was fitted by a Lorentzian function. By this method, changes in the crystal-field splitting smaller than 0.1 eV could be identified unambiguously.

For quantitative analysis, the Ti L_{23} edge is separated into four peaks by multi-peak Lorentzian fitting. Other fitting models, such as δ functions,[19] could also be used. The coefficient of determination (R^2) of the Lorentzian fitting is better than 0.99 in this paper, which means that the Lorentzian function is a reasonable model for the separation of Ti L_{23} peaks. For bulk $BaTiO_3$ (see Fig. 3), the crystal-field splitting of the Ti L_{23} edge amounts to only about 2.15 eV. Therefore, a high-energy resolution is necessary to detect variations in the crystal-field splitting. The variation in the crystal-field splitting across the $BaTiO_3$ layer is shown in Fig. 3, where the abscissa gives the relative distance from the center of the $BaTiO_3$ layer. Note that the crystal-field splitting of the L_3 edge is obtained more accurately than that of the L_2 edge due to sharper peaks, more accurate pre-edge background fitting,

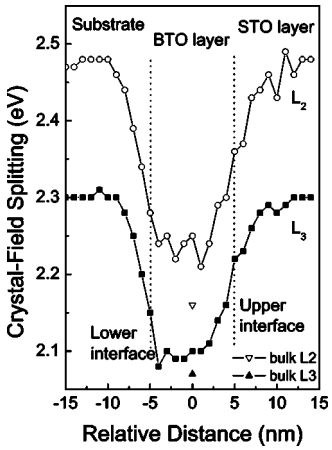

FIG. 3. Crystal-field splitting in the L_3 and L_2 edges across the $BaTiO_3$ layer. The vertical dotted lines indicate the interface positions. Additionally, the measured values for bulk $BaTiO_3$ are given (triangles).

and negligible plural scattering artifacts. The crystal-field splitting of the Ti L_2 edge is slightly larger (by ~0.18 eV) than that of the Ti L_3 edge in all layers. According to the results of crystal-field multiplet calculations of the Ti L_{23} edge for octahedral coordination of Ti with oxygen atoms,[21] this small discrepancy is due to the different effect of the crystal field on the L_3 and L_2 edges. In Fig. 3, one can see that the crystal-field splitting smoothly varies over a distance of about 5 nm at the lower interface as well as about 7 nm at the upper interface, i.e., the lower interface is sharper than the upper interface. This finding is in agreement with the TEM results of Visinoiu *et al.*[12] The different roughnesses of the interfaces may be due to a difference in the morphological stability of the growth surfaces caused by different surface energies. The smooth variation of the crystal-field splitting at either interface is mainly caused by the instrumental broadening and inelastic scattering in the specimen. The instrumental broadening is related to the probe size, the thickness of the specimen t, the convergent semiangle α, and the collection semiangle β. The probe size of the used STEM is about 0.4 nm, which is much smaller than the varying distance. The convergent and collection angles play the important roles in the instrumental broadening. According to the integrated intensity ratio between the zero-loss peak and the low-loss region of the spectrum,[13] the estimated relative thickness of the region for acquiring the core-loss spectra is about 0.43 inelastic mean-free path. The absolute thickness of the specimen can be roughly estimated at 43 nm.[13] We use the equation $2t \times \tan[\max(\alpha, \beta)]$ to estimate the instrumental broadening. In this case, $t=43$ nm, $\alpha=14$ m rad, and $\beta=12$ m rad, and the estimated instrumental broadening is about 1.2 nm. The Bethe-ridge angle indicates the maximum of the inelastic scattering angle, which can be estimated by $\sqrt{E/E_0}$, where E is the energy loss, and E_0 is the energy of the incident electron.[14] For the Ti L_{23} edges, $E=456$ ev and $E_0=100$ keV, the Bethe-ridge angle is about 68 m rad, which can reduce the spatial resolution to about 2.8 nm. Otherwise, if the incident beam is not absolutely parallel to the interface, additional broadening can be introduced. Additionally, the crystal-field splitting of the $BaTiO_3$ layer is a little larger with respect to that of bulk $BaTiO_3$. This difference can be interpreted by the internal strain, which compresses the octahedra to reduce the Ti–O bond length. As known, the shorter the Ti–O bond length, the stronger the crystal field is, which finally leads to the larger crystal-field splitting.

Figure 4 shows the L_{23} edge of Ti^{4+} with differently distorted octahedral coordinations. The octahedra share two edges with other octahedra in rutile, three edges in brookite, and four edges in anatase. They share six corners in the perovskite structure. In the distorted cubic crystal field, the second main peak (e_g in the L_3 edge) is split into two peaks. Using atomic multiplet theory, including the crystal field, de Groot *et al.* calculated the Ti^{4+} L_{23} edge in O_h and D_{4h} symmetries, respectively.[18] No such splitting was found in O_h symmetry. The reproduced splitting of the L_3 e_g peak in D_{4h} symmetry was in good agreement with the experimental spectra of rutile TiO_2, even though the octahedron in rutile is actually of D_{2h} symmetry. Therefore, this splitting is believed to be related to the distortion of the octahedral coordinations. With respect to molecular orbitals, the low-energy

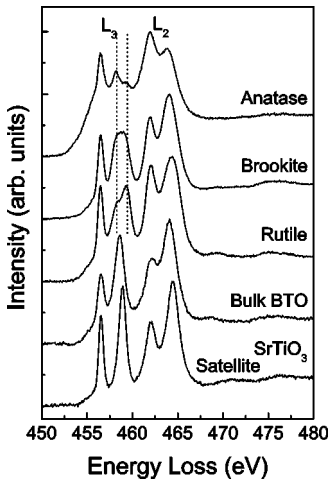

FIG. 4. Experimental spectra of bulk BTO and STO compared to TiO_2 anatase, brookite, and rutile. The splitting of the e_g peak in the L_3 edge is indicated by vertical dotted lines. Satellite structures appear above the white lines.

orbitals point to the ligands with longer bond lengths, while the high-energy orbitals point to the ligands with shorter bond lengths. In bulk BTO, the octahedron is in a D_4 symmetry, which can be regarded as a distortion of the D_{4h} symmetry. But a splitting has never been observed in the Ti L_3 e_g edge, neither in the experimental spectra of BTO layers nor in spectra of bulk BTO. This unidentified splitting in BTO might be due to the following reasons:

(1) The splitting in perovskite titanate ceramics is too small to be separated in our spectrometer, or core-hole lifetime broadening and instrumental broadening smear out the small splitting.

(2) The effect of crystal-field splitting in the edge-sharing structures is stronger than that in the corner-sharing structures. The low-energy peak relates to the shared edges, while the high-energy e_g peak relates to the ligand atoms. The relative intensity of the low-energy peak increases with the number of shared edges from rutile to anatase. The splitting of the e_g peak may be also difficult to observe in other similar perovskite titanate ceramics, such as $PbTiO_3$ or $ZrTiO_3$, due to above reasons. Fig. 5(a) shows the spectra taken at the BTO/STO interface and in the 10-nm-thick $BaTiO_3$ layer. Spectra taken from $SrTiO_3$ (substrate) and bulk $BaTiO_3$ are also given for comparison. All of the spectra are also aligned by the first peak. The centers of the peaks are indicated by vertical dotted lines. There is no discriminable difference between the spectra from the BTO layer and from bulk BTO. The spectrum at the interface can be regarded as the superposition of the BTO layer and STO substrate spectra. Special fitting techniques, such as the multiple linear least-squares (MLLS) fitting, may be appropriate for this case.[22]

The Ti L_{23} edges can be reproduced by the first-principle full multiple-scattering (FMS) commercial code Feff8.20 (Ref. 23). An excellent review of FMS theory was given by Rehr and Albers.[24] In $SrTiO_3$, there are two satellite peaks above the Ti L_{23} edges with an energy separation of about 5.5 eV, which corresponds to the energy separation of the L_{23} edges. The Ti L_{23} edges were calculated shell-by-shell

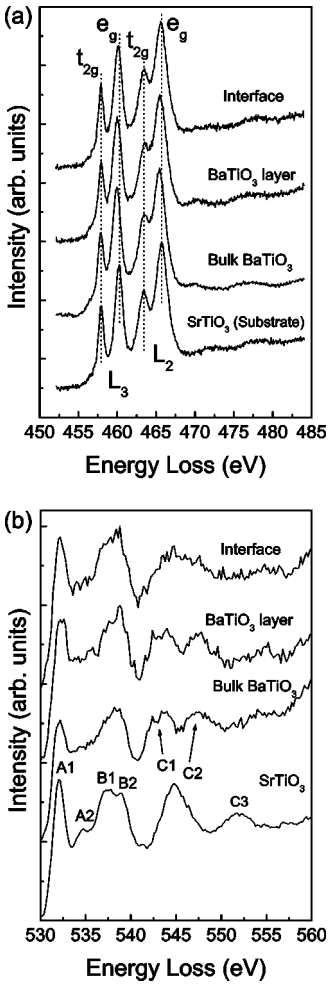

FIG. 5. (a) Comparison of the fine structure of the titanium L_{23} edge measured in STO, BTO, and at the STO/BTO interface. (b) Comparison of the fine structure of the oxygen K edge. The reference spectra measured in bulk BTO and STO were averaged by five spectra taken from different positions.

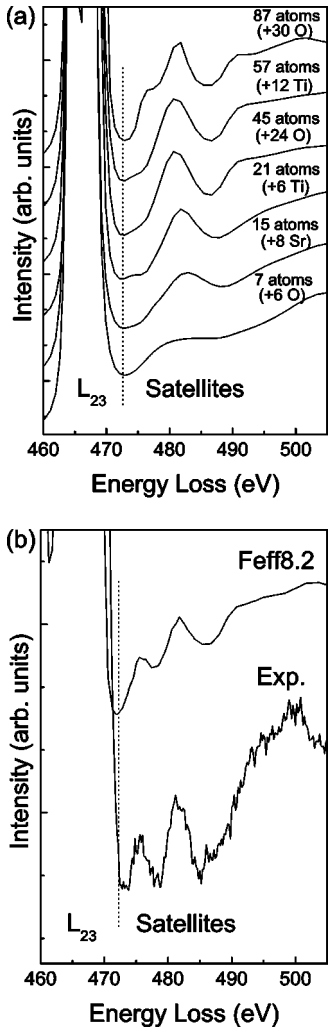

FIG. 6. (a) Satellite structures of the Ti L_2 edge of $SrTiO_3$ calculated in the shell mode of the FMS method. The spectra are labeled by the total number of the atoms in the clusters. The number of atoms in the new shell with respect to the previous cluster is indicated in parenthesis. (b) The experimental satellite structures of the Ti L_{23} spectrum compared with the FMS calculations in $SrTiO_3$.

using the FMS method [Fig. 6(a)]. The satellite structures can be well reproduced when the third shell (labeled 21 atoms) was considered in the cluster. In the simulation, the satellites of the L_{23} edges were calculated, then weighted by a branching intensity ratio (I_{L_3}/I_{L_2}) of 0.8 (Ref. 25), and then summed up. The result is in good agreement with the experimental spectrum without any manual energy shift [cf. Fig. 6(b)]. With regard to multiple scattering, the satellites originate from backscattering at neighboring atoms, and the charge transfer process dominates the satellite structures. The satellites were shifted to lower energy by about 1.5 eV in BTO with respect to bulk STO [cf. Fig. 5(a)]. This means that the longer interatomic distance leads to a smaller charge transfer. The energy shift of the satellite peaks is more significant than that of the white-line peaks. In the low energy-loss region (0–10 eV above the Fermi energy), the four main peaks can also be reproduced (not shown in the left part of the spectra in Fig. 6), but the relative intensity of the peaks is not in agreement with the experimental spectrum due to neglected multiplet effects (i.e., intraatomic interactions redistribute the intensities of the peaks), which are more important than the charge transfer process for 3*d* transition metal atoms.[26] In other words, the excited electrons with a low kinetic energy are easily localized in unoccupied 3*d* states above the Fermi level. For the simulation of the L_{23} edges of the transition-metal atoms, the agreement with the experiment can be improved not only for the main peaks but also for the satellites by the charge-transfer and multiplet (CT-M) model[27] or multichannel multiple-scattering theory.[28]

B. O K edge

The fine structure of the O K edge was acquired with an energy dispersion of 0.2 eV/channel. The acquisition time per spectrum was set to 10 s for sufficient intensity. The fine structures of the O K edge are compared in Fig. 5(b). The spectra are aligned at peak A1. The peaks A1 and A2 are related to the 3*d* orbitals of the Ti atoms. The separation between A1 and A2 amounts to about 2.4 eV, which reason-

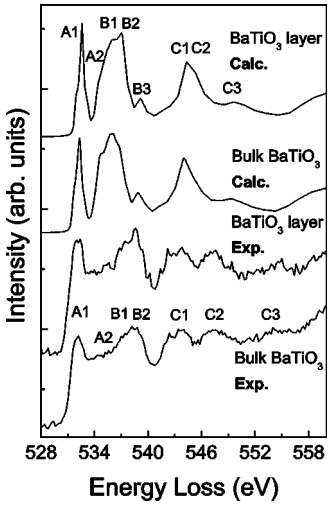

FIG. 7. Experimental and simulated oxygen K edges.

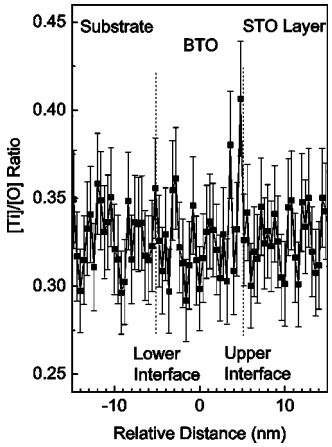

FIG. 8. [Ti]/[O] ratio across the $BaTiO_3$ layer. The vertical dotted lines indicate the upper and lower interfaces. The abscissa denotes the relative distance from the middle of the BTO layer.

ably coincides with the crystal-field splitting in the Ti L_{23} edge. The identical separation is one of the evidences of the hybridization of the oxygen 2*p* orbitals with the Ti 3*d* orbitals. This interpretation corresponds to the explanation of de Groot *et al.* in terms of ligand-field splitting.[29]

In order to identify the origin of the features B1, B2, C1, and C2, the O K edge of bulk $BaTiO_3$ was simulated by FMS calculations shell-by-shell, using the parameters given in Table I. Overlapped self-consistent muffin-tin potentials were used to reduce the effects of potential discontinuities at the muffin tins. As shown in Fig. 2(b), there are two unequal positions for oxygen atoms in the tetragonal perovskite structure, labeled O_1 and O_2. One O_1 and two O_2 oxygen atoms are included in one unit cell. The spectra from the two unequal oxygen atoms were calculated, respectively. Then the spectra were multiplied by the corresponding number of atoms in the unit cell and summed up. The results of the calculation of $BaTiO_3$ layers and bulk $BaTiO_3$, including 107 atoms in the individual cluster, are in good agreement with the main features of the experimental spectra, as shown in Fig. 7. The difference in the spectra calculated for a BTO layer and bulk BTO is very small, which agrees with the experimental results. This means that the strain-induced distortion of the BTO structure is not the main reason for the difference in the dielectric properties of a BTO layer and bulk BTO. Interface effects have to be taken into account. Peak A1 is reproduced very well in the calculations. Peak A2 is also related to the crystal-field splitting, but the intensity is very low, which is consistent with the experimental spectra. Peak B1 is the result of backscattering at the nearest oxygen shell. Peak B2 arises from scattering at the second-nearest oxygen shell. Meanwhile, peaks B1 and B2 are also strongly related to the nearest Ba shell. Peak B3 originates from the nearest Ba shell. This peak is very weak in the experimental spectra. The peaks C1 and C2 arise from scattering at the nearest oxygen shell. The experimental energy splitting between C1 and C2 amounts to about 3.8 eV. However, this splitting cannot be well reproduced in the FMS simulations. This disagreement might be caused by the fact that the polarization potential along the *c* axis is neglected in the FMS calculations of $BaTiO_3$. The polarization potential is generated by the displacement of Ti atoms in the octahedra along the same direction, which breaks the symmetry of the nearest oxygen atoms around the excited oxygen atom.[30] Peak C3 is mainly related to scattering at the third oxygen shell. In multiple-scattering calculations, the fine structures in the spectra predominantly arise from strong backscattering at neighboring oxygen atoms. Contributions from distant cations are usually small.

C. [Ti]/[O] Ratio

The [Ti]/[O] element ratio was calculated by a standard procedure which was implemented in the DIGITALMICROGRAPH software packages. The detail of the calculations can be found in Ref. 13. A 10 eV energy window in the pre-edge was used to fit the background for both core-loss edges. The integrated intensities of the Ti L_{23} edges and the O K edge were calculated up to 45 eV and 60 eV above the corresponding threshold energies, respectively. The cross sections were calculated by a Hartree-Slater method. Fig. 8 shows the element ratios across the $BaTiO_3$ layer. A slight slope caused by the non-uniform thickness due to the wedge-shaped TEM specimen has been corrected by subtracting a fitted line. A significant increase (around 6%) of the [Ti]/[O] ratio is found reproducible at several different positions at the upper interface of the $BaTiO_3$ layer, while no detectable increase is found at the lower interface. The increased [Ti]/[O] ratio implies that oxygen vacancies are aggregated at the upper interface. Similar results have been reported for grain boundaries[6,31] and dislocation cores.[9] Since the surface of the STO substrate was prepared to terminate at the TiO_2 plane,[12] the molecules were deposited at the beginning of the growth process on the STO surface in the stacking sequence BaO -TiO_2-BaO-TiO_2… due to energetic reasons. In the first few layers (<5 nm), the misfit strain from the interface makes the energetic preference strong, which causes this region to be free of defects or defects move to the upper interface. When the BTO layer becomes thicker, the misfit strain is relaxed. The oxygen-vacancy ordering mechanism may oc-

cur because the stacking sequence is not rigorous.[32] This may be one of the possible explanations for the formation of space charge layers[11] at the rough upper interface of $BaTiO_3$ layers.[12] The presence of a space charge at the upper interface dominates the difference of dielectric properties between multilayers and bulk $BaTiO_3$.

IV. SUMMARY

High-energy-resolution electron energy-loss spectroscopy has been applied to investigate $BaTiO_3/SrTiO_3$ multilayers. The near-edge fine structures are discussed based on experimental results and first-principle full multiple-scattering calculations. We found that the crystal-field splitting can be used to characterize the internal strain in $BaTiO_3$ layers. The crystal-field splitting of the $BaTiO_3$ thin layer is a little larger than that of bulk $BaTiO_3$ due to the presence of the internal strain. This result is confirmed by the lattice parameters of the $BaTiO_3$ thin layer determined by the selected area diffraction pattern, which reveals the crystal structure of the $BaTiO_3$ layer to be compressed in the growth plane by the internal strain. Otherwise, the roughness of the interfaces can be reflected on the variation of the crystal-field splitting. The satellite structures of the Ti L_{23} edges and oxygen K edge of the multilayers have been simulated by first-principle full multiple-scattering calculations, which give us a better understanding of the origin of the fine structures. The simulated spectra are consistent with the experimental results. The satellite structures of the Ti L_{23} edges and the high-energy fine structures of the oxygen K edge have been interpreted by the photoelectron-wave backscattering of the neighboring oxygen atoms instead of the electron transition from the core-loss edge to the Ti 4*s* and 4*p* states. From the increased [Ti]/[O] ratio obtained, oxygen vacancies are found to preferably aggregate at the rougher, upper interface of $BaTiO_3$ layers. We conclude that the difference of dielectric properties between multilayers and bulk $BaTiO_3$ is dominated by the aggregation of oxygen vacancies (space charges) at the rough upper interface.

ACKNOWLEDGMENTS

The authors thank C. Heiliger for providing his experimental results on TiO_2 polymorphic structures. Financial support of the Deutsche Forschungsgemeinschaft is acknowledged.

*Electronic address: leipner@cmat.uni-halle.de

[1] J. F. Scott, Ferroelectr. Rev. **1**, 1 (1998).
[2] D. E. Kotecki, J. D. Baniecki, H. Shen, R. B. Laibowitz, K. L. Saenger, J. J. Lian, T. M. Shaw, S. D. Athavale, C. Cabral, Jr., P. R. Duncombe, M. Gutsche, G. Kunkel, Y. J. Park, Y. Y. Wang, and R. Wise, IBM J. Res. Dev. **43**(3), 367 (1999).
[3] W. Grogger, F. Hofer, B. Kraus, I. Rom, W. Sitte, and P. Warbichler, Mikrochim. Acta **133**, 125 (2000).
[4] P. Moreau, N. Brun, C. A. Walsh, C. Colliex, and A. Howie, Phys. Rev. B **56**, 6774 (1997).
[5] R. Brydson, J. Bruley, H. Müllejans, C. Scheu, and M. Rühle, Ultramicroscopy **59**, 81 (1995).
[6] M. Kim, G. Duscher, N. D. Browning, K. Sohlberg, S. T. Pantelides, and S. J. Pennycook, Phys. Rev. Lett. **86**, 4056 (2001).
[7] S. B. Lee, W. Sigle, and M. Rühle, Acta Mater. **50**, 2151 (2002).
[8] S. Stemmer, S. K. Streiffer, N. D. Browning, C. Basceri, and A. I. Kingonbrowning, J. Colloid Interface Sci. **8**, 209 (2000).
[9] Z. Zhang, W. Sigle, and M. Rühle, Phys. Rev. B **66**, 094108 (2002).
[10] Z. L. Zhang, W. Sigle, W. Kurtz, and M. Rühle, Phys. Rev. B **66**, 214112 (2002).
[11] Y. Yoneda, K. Sakaue, and H. Terauchi, Jpn. J. Appl. Phys., Part 1 **39**, 4839 (2000).
[12] A. Visinoiu, R. Scholz, S. Chattopadhyay, M. Alexe, and D. Hesse, Jpn. J. Appl. Phys., Part 1 **41**, 6633 (2002).
[13] R. F. Egerton, *Electron Energy-Loss Spectroscopy in the Electron Microscope* (Plenum Press, New York and London, 1996), Chap. 4.
[14] D. B. Williams and C. B. Carter, *Transmission Electron Microscopy* (Plenum Press, New York, 1996), Chap. 37.
[15] H. T. Evans, Acta Crystallogr. **4**, 377 (1951).
[16] G. M. Meyer, R. J. Nelmes, and J. Hutton, Ferroelectrics **21**, 461 (1978).
[17] M. E. Lines and A. M. Glass, *Principles and Applications of Ferroelectrics Related Materials* (Clarendon, Oxford, 1977).
[18] F. M. F. de Groot, J. C. Fuggle, B. T. Thole, and G. A. Sawatzky, Phys. Rev. B **41**, 928 (1990).
[19] R. D. Leapman and L. A. Grunes, Phys. Rev. Lett. **45**, 397 (1980).
[20] B. T. Thole and G. van der Laan, Phys. Rev. B **38**, 3158 (1988).
[21] A. Strecker, U. Salzberger, and J. Mayer, Prakt. Metallogr. **30**, 482 (1993).
[22] R. Door and D. Gängler, Ultramicroscopy **58**, 197 (1995).
[23] A. L. Ankudinov, C. E. Bouldin, J. J. Rehr, J. Sims, and H. Hung, Phys. Rev. B **65**, 104107 (2002).
[24] J. J. Rehr and R. C. Albers, Rev. Mod. Phys. **72**, 621 (2000).
[25] R. D. Leapman, L. A. Grunes, and P. L. Fejes, Phys. Rev. B **26**, 614 (1982).
[26] F. M. F. de Groot, J. Electron Spectrosc. Relat. Phenom. **67**, 529 (1994).
[27] K. Okada and A. Kotani, J. Electron Spectrosc. Relat. Phenom. **62**, 131 (1993).
[28] C. R. Natoli, M. Benfatto, C. Brouder, M. F. Ruiz López, and D. L. Foulis, Phys. Rev. B **42**, 1944 (1990).
[29] F. M. F. de Groot, M. Grioni, J. C. Fuggle, J. Ghijsen, G. A. Sawatzky, and H. Petersen, Phys. Rev. B **40**, 5715 (1989).
[30] J. V. Mantese, N. W. Schubring, A. L. Micheli, and A. B. Catalan, Appl. Phys. Lett. **67**, 721 (1995).
[31] I. Leivin, R. D. Leapman, and D. L. Kaiser, J. Mater. Res. **15**(7), 1433 (2000).
[32] J. F. Scott and M. Dawber, Appl. Phys. Lett. **76**, 3801 (2000).